1
1

2

High Pressure Effects on the Iron-Iron Oxide and Nickel-Nickel Oxide Oxygen Fugacity Buffers

5

6

Andrew J. Campbell [a,*], Lisa Danielson [b], Kevin Righter [b], Christopher T. Seagle [c], Yanbin Wang [d], and Vitali B. Prakapenka [d]

[a] Department of Geology, University of Maryland, College Park, MD 20742 USA

[b] Johnson Space Center, NASA, Houston, TX 77058 USA

[c] Department of the Geophysical Sciences, University of Chicago, Chicago, IL 60637 USA

[d] Consortium for Advanced Radiation Sources, The University of Chicago, Argonne, IL 60439 USA

15

*Corresponding author. Tel: +1 301 405 4086; fax: +1 301 314 9661

Email address: ajc@umd.edu (A. J. Campbell)

18

19

2

3

22   **Abstract**

23

24   The chemical potential of oxygen in natural and experimental samples is

25   commonly reported relative to a specific oxygen fugacity (fO$_2$) buffer. These buffers are

26   precisely known at 1 bar, but under high pressures corresponding to the conditions of the

27   deep Earth, oxygen fugacity buffers are poorly calibrated. Reference (1 bar) fO$_2$ buffers

28   can be integrated to high pressure conditions by integrating the difference in volume

29   between the solid phases, provided that their equations of state are known. In this work,

30   the equations of state and volume difference between the metal-oxide pairs Fe-FeO and

31   Ni-NiO were measured using synchrotron x-ray diffraction in a multi-anvil press and

32   laser heated diamond anvil cells. The results were used to construct high pressure fO$_2$

33   buffer curves for these systems. The difference between the Fe-FeO and Ni-NiO is

34   observed to decrease significantly, by several log units, over 80 GPa. The results can be

35   used to improve interpretation of high pressure experiments, specifically Fe-Ni exchange

36   between metallic and oxide phases.

37

38   *Keywords*: oxygen fugacity; high pressure; equations of state.

4   2

5

1. Introduction

The chemical potential of oxygen is frequently as important as temperature or pressure in controlling the chemical and physical behavior of minerals. Variations in the oxygen potential can cause insulator-metal transformations, for example, or drive large changes in diffusion rates and rheological properties through its control over vacancy populations. Perhaps most important to geochemical consideration, the chemical potential of oxygen can have great effect on elemental partitioning between coexisting phases, particularly when the chemical exchange involves a redox reaction.

In high-pressure, high-temperature geochemistry experiments, the oxygen fugacity (fO_2) is frequently set by, or determined in relation to, a metal-oxide fO_2 buffer (e.g., Fe-FeO, Ni-NiO, Re-ReO$_2$) (Dobson and Brodholt, 1999; Rubie, 1999). To compare the experimental results to one another, it is important to know how these buffers change with pressure; otherwise the redox dependence determined by comparison of differently-buffered experiments will be systematically in error. For example, high pressure metal-silicate reactions have been extensively studied using multi-anvil apparatus (e.g., Thibault and Walter, 1995; Li and Agee, 1996; 2001; Righter et al., 1997; Ohtani et al., 1997; Walter et al., 2000; Righter, 2003; Wade and Wood, 2005; Corgne et al., 2008; Kegler et al., 2008), and the various systems used as reference buffers in those experiments are imperfectly calibrated against one another at high pressures. Moreover, recent improvements in sample preparation techniques and microanalytical tools have turned the diamond anvil cell into a petrological tool, used to study phase relations and elemental partitioning between phases in recovered high-P,T samples (e.g., Irifune et al., 2005; Takafuji et al., 2005; Auzende et al., 2008; Riccoleau et al., 2008; Sinmyo et al., 2008). As diamond cell technology continues to advance, with improved methods for microanalysis of chemical distributions in the high-pressure samples, the chemical activity of oxygen will become an increasingly important factor for interpretation of the

6

3

66   experimental results, comparable to the important role fO_2 control plays in lower pressure

67   petrological studies. Likewise, increasingly sophisticated computer simulations of

68   chemical reactions at high pressure can be expected to advance into high-pressure

69   petrological studies. The activity of oxygen in these simulations can be varied by

70   adjusting the number of oxygen atoms in the system (e.g., Zhang and Oganov, 2006).

71   Placing these new experimental and computational results in a thermodynamic

72   framework including oxygen fugacity will greatly facilitate the understanding of the

73   results, and also permit separate experiments to be more usefully compared to one

74   another.

75   Oxygen fugacity (fO_2) is a proxy for the chemical activity of oxygen (a_{O2}) in a

76   system. For the general metal-oxide equilibrium reaction

77   (1) $M + {}^x/_2\, O_2 = MO_x$

78   the fO_2 is related to the Gibbs energies (G) by

79   (2) ${}^x/_2\, RT \ln fO_2 \ = \ G(MO_x) - G(M) \ = \ \Delta G$

80   where ΔG is the difference in Gibbs energy between the oxide (MO_x) and metal (M)

81   phases. The pressure effect on the fO_2 buffer is thus related to the change in ΔG with

82   pressure. Along each isotherm, $\partial G/\partial P|_T = V$, so the effect of pressure on fO_2 depends on

83   the volume difference (ΔV) between oxide and metal:

84   (3) $\partial(\ln fO_2) \,/\, \partial P|_T \ = \ (2/xRT)\, \Delta V$

85   One can construct high pressure fO_2 buffer curves by integrating equation (3)

86   isothermally to a specified pressure, using appropriate equation of state data for each

87   phase buffering the oxygen activity (metal and oxide, in the example here). However,

88   some of the relevant equations of state are poorly known even for commonly used buffer

89   materials.

90   In this study we present high pressure, high temperature oxygen fugacity curves

91   for the Fe-FeO and Ni-NiO reactions. These buffers were chosen for their great

92   importance to deep Earth geochemical studies. The Fe-FeO reaction dominates the redox

93   conditions of the deep Earth because of the association of the metallic core with a mantle

94   containing significant amounts of oxidized iron. Consequently, many high pressure

95   geochemical experiments are performed under conditions close to this buffer. Likewise,

96   the Ni-NiO buffer is widely used to produce more oxidizing conditions in geochemical or

97   petrological experiments. Of particular importance are studies of metal-silicate

98   partitioning, that are carried out to understand the observed budget of moderately and

99   highly siderophile elements in the mantle. Nickel is a key trace element in these studies,

100   because its well-constrained mantle abundance (McDonough and Sun, 1995) is thought

101   to be a consequence of metal-silicate equilibration during core-mantle segregation in the

102   early Earth (Li and Agee, 1996; Ohtani et al., 1997).

103   To determine these high pressure buffer curves, we propagate the well-established

104   1 bar buffers to high pressure using equation (3). The high-P,T values of ΔV that we use

105   are determined experimentally by in situ X-ray diffraction measurements of the metal-

106   oxide pairs coexisting under identical high-P,T conditions. Comparing V between two

107   independently measured equations of state compounds the errors associated with them.

108   Therefore, we measured coexisting metal-oxide buffer pairs simultaneously, which

109   minimizes systematic biases that might appear between separate studies and improves the

110   precision of the ΔV data used to determine the high pressure fO_2 buffers. A wide range of

111   P,T conditions, exceeding 65 GPa and 2400 K, was covered by the use of two different

112   high-pressure technologies, the multi-anvil press (MAP) and the laser-heated diamond

113   anvil cell (DAC).

114

115

116

2. Experimental

2.1. Multi-anvil press

The multi-anvil press (MAP) samples were prepared in the Johnson Space Center high-pressure laboratory. The sample materials were mixtures of 1:1 by weight of Ni:NiO or Fe:Fe$_{1-x}$O, all obtained from Alfa Aesar. These were then mixed with 50% NaCl by weight, which acted as an internal pressure standard and also helped to distribute the sample material, inhibiting excessive grain growth that would deleteriously affect the x-ray diffraction measurements. Each high-P,T run included either Ni:NiO or Fe:Fe$_{1-x}$O, not both. The sample mixtures were loaded into a boron nitride capsule and set into either a 14/8 or 10/5 octahedral MAP assembly. These octahedral assemblies were developed by the COMPRES multi-anvil assembly initiative, and were designed specifically for use in synchrotron-based multi-anvil experiments (Leinenweber et al., 2006). The 14/8 G2 in situ assembly is a graphite box furnace with a forsterite insulating sleeve. The heater and sleeve were x-ray transparent, easily permitting x-ray diffraction measurements, but heating was limited to < 1000 °C, < 13 GPa to avoid graphite-to-diamond conversion. The 10/5 in situ assembly expanded the pressure range achievable, and temperature was limited by melting of the NaCl. X-ray transmission through the Re foil heaters was allowed by fabricated small slits aligned with Al$_2$O$_3$ windows in the LaCrO$_3$ insulating sleeve. This allowed x-ray transmission through the sample chamber, but introduced Al$_2$O$_3$ diffraction peaks in the measured spectrum.

The octahedral assemblies were loaded into the 1000-ton multi-anvil press at beamline 13-ID-D of the GSECARS sector of the Advanced Photon Source (Uchida et al., 2002). The samples were oven dried before loading them into the press. They were then pressurized for in situ, high-P,T X-ray diffraction using synchrotron radiation. The x-ray source was a white beam, collimated to approximately 100 μm x 100 μm using two

144   pairs of WC slits. Diffracted X-rays were measured using a Ge solid state energy

145   dispersive detector at a fixed angle of 6.1˚. The detector had 4000 channels, and the

146   exposure times were typically 5 minutes.

147   In most experiments, the sample was pressurized to its maximum pressure (~12

148   GPa in these experiments) before any equation of state data were collected. Then the

149   sample was heated to the maximum target temperature, which caused some reduction of

150   pressure. Pressure-volume-temperature (P-V-T) diffraction data were collected on

151   cooling cycles, when non-hydrostatic stresses had been relaxed. After each cooling cycle,

152   the press load was reduced, the sample was heated, and data collection resumed on the

153   next cooling cycle. Data were collected in temperature intervals of 200 ˚C.

154   The detector angle was calibrated using the zero pressure lattice spacing of NaCl

155   (a = 5.6402 Å, JCPDS card #05-0628), measured from each sample before initial

156   compression. The recorded x-ray diffraction patterns were analyzed using PeakFit (Systat

157   Software, Inc.); this involved background subtraction and peak fitting, including

158   deconvolution of overlapping peaks. In addition to the sample materials, the NaCl

159   pressure standard, and the Al_2O_3 windows, both diffraction and x-ray fluorescence from

160   the Re foil heaters were sometimes detected. Lattice parameters were calculated from at

161   least 3 lines for all samples of hexagonal symmetry, and at least 2 lines for isometric

162   samples. Uncertainties on the lattice parameters reflect standard deviations from multiple

163   diffraction peaks. Pressures were determined from the Decker equation of state for the B1

164   phase of NaCl (Decker, 1971).

165   Stoichiometric FeO is only stable at high P and T; at lower pressures and

166   temperatures non-stoichiometric wüstite is observed, with variable composition, even

167   when coexisting at equilibrium with Fe metal (Stølen and Grønvold, 1996). We used

168   ΔV_{IW} data only from the P-T range in which stoichiometric FeO coexisted with fcc-Fe

169   according to the model B phase diagram of Stølen and Grønvold (1996); their model B

170   was chosen because the bulk modulus values in that model are consistent with those in

171   Fei (1996) and Haavik et al. (2000), and also the bulk modulus determined in the present

172   study. Stølen and Grønvold's (1996) result is that FeO coexisting with Fe metal is

173   stoichiometric above 5 GPa at 900 K, with a slope < -120 K/GPa.

174

175   *2.2. Laser-heated diamond anvil cell*

176

177   The diamond anvil cell (DAC) samples were prepared in the University of

178   Maryland Laboratory for Mineral Physics. The sample materials were mixtures of either

179   Ni-NiO or $Fe\text{-}Fe_{1-x}O$, using similar materials as were used in the MAP experiments, and

180   were finely ground to ~1 μm grain size in an agate mortar. These mixtures were

181   compressed into a thin flake, approximately 3-6 μm in thickness (which may further

182   decrease by tens of percent at high compression), and then loaded into the sample

183   chamber of a symmetric-type DAC, between layers of NaCl insulator. The gaskets were

184   stainless steel or rhenium, 250 μm thick before indentation. Anvils having culet

185   diameters of 250 to 400 μm were used, and holes of 80 to 130 μm were formed in the

186   center of the preindented gaskets using an EDM (Hylozoic Products, Inc.).

187   Synchrotron X-ray diffraction measurements (Figure S1 in the Supplementary

188   Material) were carried out while laser-heating the samples at beamline 13-ID-D of the

189   GSECARS sector of the Advanced Photon Source. Details of the optical system are given

190   by Shen et al. (2005). The X-ray source was a monochromatic beam ($\lambda = 0.3344$ Å)

191   measuring 5 μm x 5 μm, and diffracted x-rays were recorded using a MAR345 CCD area

192   detector. The sample-to-detector distance was calibrated by 1 bar diffraction of CeO_2.

193   Exposure times were typically 5 s.

194   The samples were heated on both sides using a Nd:YLF laser operating in either

195   TEM_{00} or TEM_{01*} mode. The laser spot sizes were 30-40 μm, much larger than the X-ray

196   beam, and were coaligned with the beam by taking advantage of X-ray induced

197   fluorescence from the NaCl insulator. Laser powers were adjusted to equalize the

198   temperature on the two surfaces of the sample, usually to within <50 K. Temperatures

199   were measured from 5 μm diameter areas in the center of the laser heated spots on both

200   side of the sample. The spectroradiometric method (Heinz and Jeanloz, 1987) was used,

201   with the graybody approximation, over the 600-800 nm range of thermal emission. The

202   precision of fit to the thermal emission spectra was typically better than 1%; as discussed

203   by Kavner and Panero (2004) and Campbell et al. (2007), the greatest contribution to

204   uncertainty in the temperature measurements is the presence of thermal gradients,

205   especially in the axial direction through the thickness of the sample. Based on the thermal

206   modelling of Campbell et al. (2007), we estimate that the average temperature of the

207   sample within the region probed by X-ray diffraction is typically 3% less than the

208   measured surface temperatures, for the experimental parameters used in these

209   measurements. Accordingly, our reported temperatures have been corrected by –3% (0.03

210   x (T_{meas} – 295 K)), and an uncertainty equal in magnitude to this correction has also been

211   applied to our error estimates.

212   The use of X-ray diffraction during the high-P,T experiment permits pressure

213   determination by an internal standard, whose high-P,T equation of state is known. In

214   these experiments we use the NaCl insulator as a pressure standard. The advantages of

215   this are that the equations of state of both the low-pressure (B1) and high pressure (B2)

216   phases of NaCl are well determined under high-P,T conditions (Decker, 1971; Fei et al.,

217   2007), and also that the same material is then used in all of the Fe-FeO and Ni-NiO

218   experiments reported here, whether in the MAP or the DAC. A disadvantage of using the

219   insulator as the pressure standard is that the mean temperature of the standard is then not

220   equal to the mean temperature of the sample, because of the temperature gradient across

221   the NaCl layer from the hot sample surface to the cool (approximately 295 K) diamond

222   anvil surface. However, as demonstrated below and in Mao et al. (2007), the uncertainties

223   of this method are only a couple of GPa or less, so the resulting P-V-T measurements are

224   well constrained for our present purpose.

225   The temperature distribution in the sample and the NaCl insulator during laser

226   heating is schematically illustrated in Figure 1. The distribution within the sample was

227   calculated from the diffusion equation, with a gaussian distribution imposed on the

228   sample surfaces as boundary conditions (Campbell et al., 2007). The temperature

229   gradient across the NaCl layers, in the region probed by the X-ray beam, lies between

230   T_{meas} at the sample surface to T_{anvil} at the anvil surface, and the average temperature over

231   which X-rays are diffracted from the pressure medium, T_{NaCl}, is $(T_{meas}-T_{anvil})/2$. Departures

232   from linearity of this gradient may result from several sources, including: non-constant

233   diffusion coefficient of thermal diffusion in NaCl with varying temperature; radiative

234   heat transfer; and radial heat flow from the central axis to the cooler surrounding region.

235   These factors are small, and partly compensating for one another. We assume the

236   midpoint between sample surface and anvil surface temperatures to be the mean

237   temperature of the pressure standard; the sample temperature is measured

238   spectroradiometrically, and the anvil temperature must lie between room temperature

239   (295 K) and T_{meas}: $T_{anvil} = (T_{meas}+295)/2 \pm (T_{meas}-295)/2$. Therefore, as illustrated in Figure

240   1, the effective temperature through the NaCl medium can be taken to be

241   (4) $T_{NaCl} = (3T_{meas}+295)/4 \pm (T_{meas}-295)/2$

242   This translates to a typical error in pressure of only 2-6%, because of the high

243   compressibility of NaCl relative to its thermal expansion. Separate, unpublished, tests of

244   this method of calibration using a Pt sample (whose equation of state is calibrated against

245   NaCl by Fei et al., 2007) confirm that Equation (4) yields an appropriate measure of

246   pressure in the sample geometry of Figure 1.

247   Deviatoric stresses are significant in an unheated diamond anvil cell at room

248   temperature; however, at high temperatures these stresses are minimized by relaxation of

249   the sample and pressure medium (Kavner and Duffy, 2001). Under these high

250   temperature conditions, the assumption of mechanical equilibrium (i.e., constant pressure

251   between the metal, oxide, and pressure standard) is reasonable. However, our results

252 below show that at low temperature, following rapid quench of the laser heated sample,

253 residual strains remain in the cell and the assumption of mechanical equilibrium may no

254 longer hold, as also observed by Kavner and Duffy (2001).

255   **3. Results**

256

257   Tables S2 and S3 of the Supplementary Material contain the *P-V-T* data for the

258   Fe-FeO and Ni-NiO experiments respectively. Each table contains: the molar volumes of

259   each phase (metal, oxide, and NaCl pressure standard); the corresponding ΔV (= V_{ox}-V_{met});

260   the temperatures of the sample and the NaCl (corrected as in Section 2.2); and the

261   pressure determined from the equation of state of NaCl (Decker, 1971; Fei et al., 2007).

262   In Table S2, the structure of the Fe phase (fcc or hcp) is also indicated. Only those

263   phases that were stable under the indicated *P*,*T* conditions (Shen et al., 1998) are

264   included; occasionally a metastable phase of Fe was observed, but these molar volumes

265   are not reported. All reported data have FeO in the B1 structure. The high-pressure

266   rhombohedral phase of wüstite (Fei and Mao, 1994) exists only at temperatures lower

267   than those needed for our intended application of constructing high-pressure fO_2 buffers.

268   At high pressures and high temperatures a B8-type phase of $Fe_{1-x}O$ has been reported (Fei

269   and Mao, 1994; Murakami et al., 2004), but this phase was not seen in our results nor in

270   those of Seagle et al. (2008). We speculate that this could be because of the stoichiometry

271   of our FeO phase (*x* = 0). In addition to the data listed in Table S2, our analysis includes

272   the *P-V-T* data from Seagle et al. (2008), who used virtually identical experimental

273   methods in their DAC study of the Fe-FeO system. The molar volumes of Fe and FeO are

274   plotted in Figure 2, and the corresponding ΔV_{IW} is plotted in Figure 4. Although MAP

275   experiments can be performed at a predetermined temperature, controlled by feedback

276   from the thermocouple, laser-heated DAC experiments do not so easily permit a tightly

277   specified temperature, and the temperature values are usually determined after the fact.

278   For this reason, the data in the figures are coded by temperature range, rather than plotted

279   as sets of isothermal data.

280   In Table S3, all of the Ni data refer to the fcc structure, and all of the NiO data

281   refer to the B1 structure. No other phases were observed. The molar volumes of Ni and

282   NiO at high pressure and temperature are plotted in Figure 3, and the ΔV_{NNO} values are

283   plotted in Figure 4.

284

285

4. Discussion

4.1. Equations of state and $\Delta V_{ox\text{-}met}$ at high pressures and temperatures

In many geophysical applications, the difference in molar volume (or density) between phases is more important than the absolute volumes (or densities) of those phases. The application that we intend for the present data, calculating the thermodynamics of chemical equilibria at high pressure, is one example. In these cases, there are significant advantages to measuring the two phases simultaneously, under identical P,T conditions, rather than comparing two independently determined equations of state to one another. Equation of state studies can suffer from systematic biases resulting from their experimental procedures. For example, pressure standards are not all perfectly consistent with one another. Although there is ongoing work in improving this situation by comparing pressure standards to one another (Fei et al., 2007; Dorogokupets and Oganov, 2007; Dewaele et al., 2008), there is already a voluminous literature in which various, inconsistent pressure scales were used. When it is critical to compare the volumes of two phases directly, a better strategy is to measure them simultaneously to avoid problems related to inconsistency in pressure standards. Furthermore, holding the two phases together under high P,T conditions allows them to reach chemical equilibrium with one another. This is a very important advantage when there is a new phase, or new stoichiometry, that exists in the system only at high P and T, and not under ambient conditions. This is the case in the Fe-FeO system. At 1 bar the stoichiometric $Fe_{1.00}O$ phase is not stable, but at high-P,T conditions non-stoichiometric wüstite can react with metallic Fe to form $Fe_{1.00}O$ (Stølen and Grønvold, 1996); this fact was exploited in the present study. For all of these reasons, we chose to measure $\Delta V_{ox\text{-}met}$ in the Fe-FeO and Ni-NiO systems by simultaneous measurement of the molar volumes of metal and coexisting oxide at high pressures and temperatures. This strategy improves the precision to which

313   the ΔV values are determined, thereby improving the calculation of oxygen fugacity

314   buffers at high pressure.

315   High pressure, high temperature equations of state were derived for each phase by

316   fits to the combined MAP and DAC data. A Mie-Grüneisen equation of state was used,

317   (5) $P = P_{295}(V) + (\gamma/V) [E(\theta_D,T) - E_{295}(\theta_D,295)]$

318   with the 295 K isotherm (P_{295}) described by a Birch-Murnaghan equation and the thermal

319   pressure term based on a Debye model of vibrational energy (E), with Grüneisen

320   parameter $\gamma = \gamma_0(V/V_0)^q$ and Debye temperature $\theta_D = \theta_0(V/V_0)^{-\gamma}$. Although this formalism

321   does not explicitly include parameters for anharmonic or electronic contributions, it is

322   identical to that used to describe the NaCl-B2, Pt, Au, and Ne equations of state by Fei et

323   al. (2007). Parameters used in the least-squares fits to the equation of state data are

324   presented in Table 1. We do not offer an alternative set of equation of state parameters for

325   hcp-Fe, because no fit to our data was superior to the Dewaele et al. (2006) equation, so

326   we used it in our analysis instead. (The agreement between our data and the Dewaele et

327   al. (2006) equation for hcp-Fe is further evidence that the NaCl pressure medium can act

328   as an effective pressure standard, as described above, during high temperature laser

329   heating experiments when stress gradients have been relaxed.)

330   By combining data from the two different experimental methods (MAP and

331   DAC), we were able to investigate a more complete range of pressures and temperatures

332   than either method can cover alone. In principle this approach provides a more robust

333   equation of state, but one potential concern is that two different pressure standards were

334   used among the measurements (NaCl-B1 for low pressures; NaCl-B2 for high pressures).

335   Residuals from the fitted equations of state in Table 1 do not reveal systematic biases

336   between the two methods or between the two pressure calibrations. However, this may

337   simply be a consequence of there being little overlap in P,T conditions covered by the

338   two methods, and larger uncertainties related to the thermal gradient across the NaCl

339   standard in the laser heated DAC experiments. Overlapping measurements at low

340 pressure and high temperature were precluded by melting of the NaCl standard, so direct

341 comparisons cannot easily be made between the complementary but separate data sets.

342 The present results therefore rely on the accuracy of the widely used equation of state of

343 NaCl-B1 (Decker, 1971) and the fact that the NaCl-B2 equation of state has been cross-

344 calibrated against multiple other P-V-T standards (Fei et al., 2007).

345 Volume differences (Figure 4) between NiO and Ni, ΔV_{NNO}, and between FeO and

346 Fe, ΔV_{IW}, are also included in Tables S2 and S3. There is no functional form that one

347 should expect the ΔV-P-T data to follow, so the ΔV data were not fit to an equation.

348 Instead, in the calculations below the ΔV values were determined numerically from the

349 fitted equations of state given in Table 1; the volumes at each pressure and temperature

350 were determined iteratively to a precision of $<10^{-4}$ GPa in pressure.

351

352 *4.2. Calculation of high pressure buffers*

353

354 In this section we use the analyses of ΔV-P-T data in Section 4.1 to calculate the

355 NNO and IW (strictly, Fe-FeO) oxygen fugacity buffer curves at high pressures. The

356 calculations proceed by integration of Eqn. (3), with $x=1$ for both FeO and NiO:

357 (6) $\qquad \log fO_2 \;=\; \log fO_2(1 \text{ bar}) + (0.8686/RT) \int \Delta V \, dP$

358 where the conversion from ln to $\log_{10}$ was made. The 1 bar fO_2 buffers were calculated

359 using the thermodynamic data in Chase (1998) for stoichiometric FeO and Knacke et al.

360 (1991) for NiO. Only ΔG data below the melting points were used, but extrapolations of

361 these data to higher temperatures was made to facilitate analysis of high-P,T data. High

362 pressure fO_2 buffer curves were calculated along a set of isotherms from 1000 K to 2600

363 K, in 100 K intervals. Integration of $\Delta V \, dP$ for each metal-oxide system utilized the ΔV

364 values calculated from the equations of state above. For the IW system, integration

365 proceeded using the fcc-Fe data up to the fcc-hcp transition pressure (Shen et al., 1998) at

366   each temperature; above this transition pressure the ΔV_{IW} data for hcp-Fe were used in the

367   integration.

368   The IW buffer at 1 bar and at high pressures is shown in Figure 5a. Tabulated

369   values at smaller pressure increments are presented in Table S4 in the Supplementary

370   Material. There are two primary effects of pressure on the IW fO_2 curve. The first is that

371   the absolute fO_2 values increase with pressure at each temperature. The second effect is

372   that the slope $\partial(\ln fO_2) / \partial T|_P$ decreases with pressure, eventually becoming a slope of

373   approximately zero at 60 GPa, and negative at higher pressures. At pressures higher than

374   60 GPa, the slope of the oxygen fugacity curve with T is negative, so at a fixed fO_2,

375   increasing temperature drives Fe toward oxidation. This is the opposite of the behavior

376   familiar at 1 bar or other low-pressure conditions, and is not specific to the Fe-FeO

377   buffer. Any oxygen fugacity buffer will eventually obtain a negative $\partial(\ln fO_2) / \partial T|_P$ slope

378   at high pressure, because the pressure derivative $\partial(\ln fO_2) / \partial P|_T$ is greater at low

379   temperatures than it is at high temperatures, following Equation (3).

380   The analogous calculation for the NNO buffer curves at 1 bar and at high

381   pressures is illustrated in Figure 5b (calculated values in Table S5 of Supplementary

382   Material). These curves are always higher than the IW buffer curves at the same pressure,

383   reflecting the higher siderophility of Ni relative to Fe. However, the pressure effect on the

384   NNO buffer is not as great as that for the IW buffer, because ΔV_{NNO} is smaller than ΔV_{IW}.

385   Consequently, the difference between the NNO buffer and the IW buffer decreases with

386   pressure. For example, at 1500 K this difference is 4.78 log fO_2 units at 1 bar but only

387   2.38 log fO_2 units at 60 GPa. One way to view this is that Ni becomes less siderophile

388   with increasing pressure.

389   To illustrate more explicitly how the difference between the buffer curves (NNO-

390   IW) varies with pressure, these values are plotted in Figure 5c. This figure allows one to

391   quickly evaluate the difference between the buffers at any P,T condition within the range

392   covered by this study. More precise values can be determined from Tables S4 and S5 in

34   17

393   the Supplementary Material, where numerical $\log fO_2$ values for the IW and NNO oxygen

394   fugacity buffers are listed, and coefficients to a polynomial fit to the $\log fO_2$ values are

395   also provided. Misfits to the equations of state produce r.m.s. values on ΔV of

396   approximately 0.03 cm³/mol for both buffers; this contributes uncertainty to the

397   calculated buffers that is proportional to P/T, reaching ±0.2 log units at 100 GPa and

398   1500 K.

399   Contrary to the low pressure circumstances, the difference between the two

400   buffers has a negative slope above ~50 GPa (Figure 5c). This implies that at high

401   pressures Ni becomes more siderophile with increasing temperature; Kegler et al. (2008)

402   noted a similar effect in their data regression, but at somewhat lower pressure, ~30 GPa.

403

404   *4.3 Applications*

405

406   As petrological and geochemical studies extend deeper into the Earth, it is

407   necessary to have a thermodynamic framework in place in which to interpret the data.

408   The present study is a step in this necessary direction, by extending two commonly used

409   buffers to great depths in the Earth and illustrating the pressure-induced changes in the

410   difference between them. One might consider how the Fe-FeO and NNO buffers relate to

411   one another along the pressure-temperature path in the Earth's deep mantle. We show this

412   comparison in Figure 6, in which the values of these two buffers are shown along a

413   representative geotherm, in this case the Brown and Shankland (1981) model. At 1 bar

414   and 1400 K, the difference between the NNO and Fe-FeO buffers is 5.0 log units. By 670

415   km (23.8 GPa by PREM (Dziewonski and Anderson, 1981) and 1873 K by Brown and

416   Shankland (1981)), this difference has dropped to 3.4 log units, and at 2000 km depth

417   (86.9 GPa, 2256 K) the difference is only 2.1 log units. This relative change in the metal-

418   oxide buffers should manifest itself in changing chemical behavior of Ni. The oxygen

419   fugacity of the mantle is largely reflected in the redox state of Fe, and there is a body of

420   evidence that much of the mantle is saturated in Fe-rich metal (Frost and McCammon,

421   2008), so the mantle fO_2 should lie just below the Fe-FeO buffer shown in Figure 6. The

422   exchange of Fe and Ni between phases will vary with depth according to the variation in

423   differences in buffers shown in the figure. One expects on this basis that Ni will be less

424   strongly siderophile at depth, relative to Fe.

425   More generally, the pressure dependence on differences in fO_2 buffers can play a

426   role in understanding, from a thermodynamic perspective, why chemical partitioning

427   behavior varies the way it does with pressure. For example, as pressure and temperature

428   increase, the NNO and IW buffer curves converge (Figure 5c); in essence, Ni becomes

429   less siderophile. Holding other factors (namely activity coefficients) equal, one would

430   then expect that with increasing pressure, the Ni-Fe exchange coefficient between metal

431   and silicate or oxide would decrease. This is in fact observed; partitioning studies

432   between liquid silicate and metal show that $K_{met/sil}^{Ni\text{-}Fe}$ decreases with increasing pressure

433   (Thibault and Walter, 1995; Li and Agee, 1996; 2001; Bouhifd and Jephcoat, 2003;

434   Corgne et al., 2008). There is an extensive literature from these experimental studies,

435   principally with the goal of understanding chemical exchange and equilibration between

436   the silicate mantle and the segregating core during early Earth differentiation.

437   Parameterizations in $P,\ T,\ fO_2$, and nbo/t have been crucial to comprehensive

438   understanding of metal/silicate partitioning (Righter et al., 2003). Evolution of these

439   parameterizations, using more robust thermodynamic treatment of the oxygen fugacity

440   states in the experiments, is a natural way to augment the existing data to improve its

441   accuracy and power of prediction, and also to better guide future experimentation.

442   Metal silicate partition coefficients ($D = X^{met}/X^{sil}$) are commonly parameterized

443   with linear dependence on temperature, pressure, oxygen fugacity, silicate polymerization

444   (*nbo/t*), and/or sulfur (X_S) and carbon (X_C) content of the metallic melt (e.g., Righter,

445   2003):

446   (7) $\log D = a + bT + c(P/T) + d \log fO_2 + e(nbo/t) + f \log (1\text{-}X_S) + g \log (1\text{-}X_C)$

447   This method has been shown to be effective at describing experimental data over the

448   range of their measurement conditions (Righter, 2003). However, extrapolations must be

449   treated with caution because of the assumed linearity. Here, we recast this equation to

450   permit nonlinear dependence on pressure:

451   (8) $\log D = \Delta G^{MMO}/(RT\ln 10) - \log(\gamma_M/\gamma_{MOx}) - {}^x/_2 \log fO_2$

452   where the most of the pressure dependence is in the ΔG^{MMO} term through equations (3)

453   and (6), although there may also be pressure dependence to the activity coefficients, γ

454   (i.e., nonzero mixing volumes). The fO_2 dependence of metal-silicate partitioning is

455   strong, and it is useful to eliminate it by considering, instead of the partition coefficient,

456   an exchange coefficient, K_D. For M-Fe exchange:

457   (9) $K_D = D(M)\,/\,D(Fe)^x = (X_M^{met}/X_{MOx}^{sil})\,/\,(X_{Fe}^{met}/X_{FeO}^{sil})^x$

458   (10) $\log K_D = {}^x/_2\,(\log fO_2^{MMO} - \log fO_2^{IW}) + \log(\gamma_{MOx}^{sil}/\gamma_M^{met})\,/\,(\gamma_{FeO}^{sil}/\gamma_{Fe}^{met})^x$

459   from equations (2) and (8).

460   We can use equation (10), combined with the high pressure values of $\log fO_2^{NNO} -$

461   $\log fO_2^{IW}$ calculated in the previous section, to predict the pressure dependence of Ni-Fe

462   exchange between metal and silicate. In Figure 7 the ratio of activity coefficients is

463   chosen to satisfy the low pressure experimental data for $K_{met/sil}^{Ni\text{-}Fe}$ between iron-rich

464   metallic melt and mafic silicate melt (Li and Agee, 1996; Ito et al., 1998), and equation

465   (10) is applied with our results on the fO_2 buffers of Ni-NiO and Fe-FeO to predict the

466   pressure dependence of $K_{met/sil}^{Ni\text{-}Fe}$. We use the Li and Agee (1996) and Ito et al. (1998)

467   studies to make this comparison, because in each of these studies the metal and silicate

468   compositions remained nearly constant (although they differ between the two data sets),

469   and both reached fairly high pressure. Two assumptions are made in this calculation.

470   First, it is assumed that the activity coefficients (or at least the ratio of activity

471   coefficients) are constant with pressure. Second, the calculation assumes that the free

472   energy differences between solid and liquid ($\Delta G_{liquid}^{MMO} - \Delta G_{solid}^{MMO}$) are equal for the Ni-

473   NiO system and the Fe-FeO system. This assumption is necessary because, although our

474   high pressure buffer curves are calculated for the solid metal-oxide systems, experimental

475   studies of metal-silicate partitioning are generally applied to liquid systems, because their

476   principal application is to elemental partitioning in the conditions of a magma ocean

477   during differentiation of the early Earth. More rigorously, including the solid-to-liquid

478   terms in deriving equation (10) produces:

479   (11) $\log K_D = {}^{x}\!/_2\, (\log fO_2{}^{MMO} - \log fO_2{}^{IW}) + \log (\gamma_{MOx}{}^{sil}/\gamma_M{}^{met})\,/\,(\gamma_{FeO}{}^{sil}/\gamma_{Fe}{}^{met})^x +$

480                     $[(\Delta G_{liquid}{}^{MMO} - \Delta G_{solid}{}^{MMO}) - x\,(\Delta G_{liquid}{}^{IW} - \Delta G_{solid}{}^{IW})]\,/\,(RT\ln 10)$

481   Equation (10) is otherwise exact, and deviations away from the prediction of this

482   equation must reflect violations of these two assumptions.

483   As shown in the figure, equation (10) accurately describes the pressure

484   dependence of $K_D{}^{Ni\text{-}Fe}$ up to approximately 10-15 GPa, when the activity coefficient ratio

485   is chosen to match the low pressure $K_D{}^{Ni\text{-}Fe}$ value. However, at higher pressures the

486   observed metal-silicate partitioning decreases more rapidly than predicted by equation

487   (10). One interpretation is that the assumption of constant activity coefficient ratios is

488   violated at high pressure, and the mixing volume of one or more species becomes

489   nonzero at high pressure. This could be related to coordination changes of these transition

490   elements, analogous to those reported in albite melts by Keppler and Rubie (1993), as

491   well as more general structural changes in the silicate melt, that are known to occur in

492   this pressure range (Williams and Jeanloz, 1988; Stebbins et al., 1995; Stixrude and

493   Karki, 2005). Kegler et al. (2008) reported a similar change in the pressure dependence

494   of $K_D{}^{Ni\text{-}Fe}$ that they attributed to coordination changes in the silicate melt, although their

495   observed change in $K_D{}^{Ni\text{-}Fe}$ behavior occurred at lower pressure (~5 GPa) than seen in

496   Figure 7. Another interpretation of the departure of the experimental data from the

497   equation (10) curve is that the solid-to-liquid correction is significant, and our

498   assumption that the free energy difference $(\Delta G_{liquid}{}^{MMO} - \Delta G_{solid}{}^{MMO})$ is everywhere equal

499   between the Ni-NiO system and the Fe-FeO system is invalid. In this case the pressure

500   dependence of metal-silicate partitioning will require knowledge of the volumes of the

501   melt components, and their pressure dependence. The experimental data on melt

502   components are very limited in pressure, and these have been shown to predict the

503   pressure dependence of K_D only qualitatively (Courtial et al., 1999).

504   To illustrate the possible effect of this reformulation of the metal/silicate

505   partitioning data, we postulate the emergence of a nonzero mixing volume for the Ni-Fe

506   exchange reaction above 10 GPa, pursuant to the discussion above. As shown in Figure 7,

507   a mixing volume of -1.5 cm^3/mol satisfies the difference between our predicted high-

508   pressure behavior for $K_D^{\text{Ni-Fe}}$ and the results of Li and Agee (1996). (The suddenness of

509   the mixing volume change shown in Figure 7 is a simplification.) On the basis of linear

510   extrapolations to their experimental data, Li and Agee (1996) calculated that the Ni and

511   Co abundances in the upper mantle can be explained by partitioning during Earth's core-

512   mantle equilibration in a magma ocean at pressures between 28 and 42 GPa. Our

513   reparameterization of the $K_D^{\text{Ni-Fe}}$ data, assuming ΔV_{mixing} = -1.5 cm^3/mol (and leaving the

514   Co-Fe exchange parameterization unchanged from Li and Agee (1996)), produces the

515   same degree of partitioning at a lower pressure range, between 24 and 36 GPa. Hence,

516   this change to the parameterization of $K_D^{\text{Ni-Fe}}$ can impact the inferred pressure of core-

517   mantle equilibration.

518   The linear pressure dependence of log $K_D^{\text{Ni-Fe}}$ that is fitted empirically to high

519   pressure metal-silicate partitioning data (e.g., Li and Agee, 1996; Righter et al., 1997;

520   Righter, 2003; Corgne et al., 2008) data masks two underlying thermodynamic effects,

521   shown in equations (10) and (11). First, the pressure dependence can be understood

522   simply in terms of the volume differences between the Ni-NiO and Fe-FeO buffers, that

523   are components dissolved into the metal and silicate melts. Second, the ratios of activity

524   coefficients relevant to this mixing obtain pressure dependences (nonzero mixing

525   volumes) at pressures above approximately 10-15 GPa (Figure 7), likely in response to

526   the changing structural coordinations in the silicate melt at this pressure. Over the

527   pressure range obtained by the multi-anvil press data, the pressure dependence of K_D

528 frequently is well described by a linear term, allowing accurate interpolation and

529 description of the data over this pressure range. However, it is understood that the

530 functional form of the thermodynamic expressions driving this pressure dependence may

531 not be linear, and as illustrated by the example above, with extrapolation to higher

532 pressures and temperatures a linear parameterization will be prone to increasing

533 inaccuracy. It follows that a more thorough analysis of numerous metal-oxide buffers,

534 using their (solid and/or liquid) equations of state at high pressures, offers the prospect of

535 yielding greater resolution of volume vs. structural effects on metal-silicate partitioning

536 of moderately siderophile elements, that will provide more reliable extrapolations to deep

537 Earth conditions to better interpret observed mantle chemistry in terms of the chemical

538 effects of core-mantle segregation.

539

5. Summary

The effect of pressure on oxygen fugacity buffers is calculable to high precision, if a full high pressure, high temperature equation of state is applied for the coexisting species instead of assuming a fixed ΔV. Systematic biases between pressure calibrations of equation of state measurements can be minimized by measuring the two (metal and oxide) components together. Furthermore, this approach ensures that the metal and oxide chemically equilibrate with one another, for example driving the iron oxide component to $Fe_{1.00}O$ stoichiometry in the experiments. This method was applied here to the Fe-FeO and Ni-NiO systems, using two complementary experimental methods, a multi-anvil press and diamond anvil cells, for maximum P-T coverage.

The Ni-NiO and Fe-FeO oxygen fugacity buffers both increase with pressure, but at different rates, such that the difference between them diminishes with pressure. This change in relative $\log fO_2$ units is important to consider when comparing results from high-pressure experimental runs referenced to the Fe-FeO vs. the Ni-NiO buffers. Along the P-T path of a nominal mantle geotherm, the difference between the Ni-NiO and Fe-FeO buffers is reduced by nearly three $\log fO_2$ units over 2000 km depth in the Earth. This diminishing siderophile nature of Ni is consistent with experimental studies of metal-silicate partitioning of Ni and Fe. The formalism used here allows us to better interpret these data, emphasizing that the pressure effect on $K_D{}^{\text{Ni-Fe}}$ has two components, an intrinsic volumetric effect and a possible mixing volume term above 10 to 15 GPa related to structural changes in the silicate melt. With further study covering a variety of moderately siderophile elements, this view of high pressure geochemical behavior should permit improved extrapolations to the inferred conditions of metal-silicate equilibration during Earth's core formation.

49

50   25

References

Auzende, A.-L., Badro, J., Ryerson, F.J., Weber, P.K., Fallon, S.J., Addad, A., Siebert, J., Fiquet, G., 2008. Element partitioning between magnesium silicate perovskite and ferropericlase: New insights into bulk lower-mantle geochemistry. Earth Planet. Sci. Lett. 269, 164-174.

Bouhifd, M.A., and Jephcoat, A.P., 2003. The effect of pressure on partitioning of Ni and Co between silicate and iron-rich metal liquids: a diamond-anvil cell study. Earth Planet. Sci. Lett. 209, 245-255.

Brown, J.M., and Shankland, T.J., 1981. Thermodynamic parameters in the Earth as determined from seismic profiles. Geophys. J. Roy. astr. Soc. 66, 579-596.

Campbell, A.J., Seagle, C.T., Heinz, D.L., Shen, G., Prakapenka V.B., 2007. Partial melting in the iron-sulfur system at high pressure: A synchrotron X-ray diffraction study. Phys. Earth Planet. Inter. 162, 119-128.

Chase, M.W. Jr., 1998. NIST-JANAF Thermochemical Tables, 4th ed. J. Phys. Chem. Ref. Data Monograph No. 9, American Institute of Physics.

Corgne, A., Keshav, S., Wood, B.J., McDonough, W.F., Fei, Y., 2008. Metal–silicate partitioning and constraints on core composition and oxygen fugacity during Earth accretion. Geochim. Cosmochim. Acta 72, 574-589.

Courtial, P., Gottsmann, J., Holzeid, A., Dingwell, D.B., 1999. Partial molar volumes of NiO and CoO liquids: Implications for the pressure dependence of metal-silicate partitioning. Earth Planet. Sci. Lett. 171, 171-183.

Decker, D.L., 1971. High pressure equation of state for NaCl, KCl, and CsCl. J. Appl. Phys. 42, 3239-3244.

Dewaele, A., Loubeyre, P., Occelli, F., Mezouar, M., Dorogokupets, P.I., Torrent, M., 2006. Quasihydrostatic equation of state of iron above 2 Mbar. Phys. Rev. Lett. 97, 215504.

611 Dewaele, A., Torrent, M., Loubeyre, P., Mezouar, M., 2008. Compression curves of

612   transition metals in the Mbar range: Experiments and projector augmented-wave

613   calculations. Phys. Rev. B 78, 104102.

614 Dobson, D.P., Brodholt, J.P., 1999. The pressure medium as a solid-state oxygen buffer.

615   Geophys. Res. Lett. 26, 259-262.

616 Dorogokupets, P.I., Oganov, A.R., 2007. Ruby, metals, and MgO as alternative pressure

617   scales: A semiempirical description of shockwave, ultrasonic, x-ray, and

618   thermochemical data at high temperatures and pressures. Phys. Rev. B 75,

619   024115.

620 Dziewonski, A.M., Anderson, D.L., 1981. Preliminary reference Earth model. Phys.

621   Earth Planet. Inter. 25, 297-356.

622 Fei, Y., Mao, H.-K., 1994. In-situ determination of the NiAs phase of FeO at high

623   pressure and temperature. Science 266, 1678-1680.

624 Fei, Y., 1996. Crystal chemistry of FeO at high pressure and temperature, in: Dyar, M.D.,

625   McCammon, C., Shaefer, M.W. (Eds.) Mineral Spectroscopy: A Tribute to Roger

626   Burns. Geochemical Society, Houston, pp. 243-254.

627 Fei, Y., Ricolleau, A., Frank, M., Mibe, K., Shen, G., Prakapenka, V., 2007. Toward an

628   internally consistent pressure scale. Proc. Natl. Acad. Sci. USA,

629   doi:10.1073/pnas.0609013104.

630 Frost, D.J., McCammon, C.A., 2008. The redox state of Earth's mantle. Annu. Rev. Earth

631   Planet. Sci. 36, 389-420.

632 Funamori, N., Yagi, T., Uchida, T., 1996. High-pressure and high-temperature in situ x-

633   ray diffraction study of iron to above 30 GPa using MA8-type apparatus.

634   Geophys. Res. Lett. 23, 953-956.

635 Haavik, C., Stølen, S., Hanfland, M., Catlow, C.R.A., 2000. Effect of defect clustering on

636   the high-pressure behaviour of wüstite. High-pressure X-ray diffraction and

637   lattice energy simulations. Phys. Chem. Chem. Phys. 2, 5333-5340.

638   Heinz, D.L., Jeanloz, R., 1987. Temperature measurements in the laser-heated diamond

639   cell, in: Manghnani, M.H., Syono Y. (Eds). High-Pressure Research in Mineral

640   Physics. Terra Scientific Publishing, Tokyo / American Geophysical Union,

641   Washington. pp. 113-127.

642   Irifune, T., Isshiki, M., Sakamoto, S., 2005. Transmission electron microscope

643   observation of the high-pressure form of magnesite retrieved from laser heated

644   diamond anvil cell. Earth Planet. Sci. Lett. 239, 98-105.

645   Ito, E., Katsura, T., Suzuki, T., 1998. Metal/silicate partitioning of Mn, Co, and Ni at

646   high-pressures and high temperatures and implications for core formation in a

647   deep magma ocean, in: Manghnani, M.H., Yagi, T. (Eds.) Properties of Earth and

648   Planetary Materials at High Pressure and Temperature, Geophysical Monograph

649   101. Amer. Geophys. Union, Washington, pp. 212-215.

650   Kavner, A., Duffy, T.S., 2001. Pressure-volume-temperature paths in the laser-heated

651   diamond anvil cell. J. Appl. Phys. 89, 1907-1914.

652   Kavner, A., Panero, W. R., 2004. Temperature gradients and evaluation of thermoelastic

653   properties in the synchrotron-based laser-heated diamond cell. Phys. Earth Planet.

654   Inter. 143-144, 527-539.

655   Kegler, P. Holzeid, A., Frost, D.J., Rubie, D.C., Dohmen, R., Palme, H., 2008. New Ni

656   and Co metal-silicate partitioning data and their relevance for an early terrestrial

657   magma ocean. Earth Planet. Sci. Lett. 268, 28-40.

658   Keppler, H., Rubie, D.C., 1993. Pressure-induced coordination changes of transition-

659   metal ions in silicate melts. Nature 364, 54-56.

660   Knacke, O., Kubaschewski O., Hesselmann K., 1991. Thermochemical Properties of

661   Inorganic Substances, 2nd Ed. Springer-Verlag, Berlin.

662   Leinenweber, K., Mosenfelder, J., Diedrich, T., Soignard, E., Sharp, T.G., Tyburczy, J.A.,

663   Wang, Y., 2006. High-pressure cells for in situ multi-anvil experiments. High

664   Pressure Research 26, 283-292.

665 Li, J., Agee, C.B., 1996. Geochemistry of mantle-core differentiation at high pressure.
666   Nature 381, 686-689.

667 Li, J., Agee, C.B., 2001. The effect of pressure, temperature, oxygen fugacity and
668   composition on partitioning of nickel and cobalt between liquid Fe–Ni–S alloy
669   and liquid silicate: implications for the Earth's core formation. Geochim.
670   Cosmochim. Acta 65, 1821-32.

671 Mao, W.L., Campbell, A.J., Prakapenka, V.B., Hemley, R.J., Mao, H.-K., 2007. Effect of
672   iron on the properties of post-perovskite silicate, in: Hirose, K., Brodholt, J., Lay,
673   T., Yuen, D. (Eds.), Post-perovskite: The Last Mantle Phase Transition, AGU
674   Monograph Series. American Geophysical Union, Washington, DC, Volume 174.
675   pp. 37-46.

676 McCammon, C.A., Liu, L.-g., 1984. The effects of pressure and temperature on non-
677   stoichiometric wüstite, FexO: The iron-rich phase boundary. Phys. Chem.
678   Minerals 10, 106-113.

679 McDonough, W.F., Sun, S.-s., 1995. The composition of the Earth. Chem. Geol. 120,
680   223-253.

681 Murakami, M., Hirose, K., Ono, S., Tsuchiya, T., Isshiki, M., Watanuki, T., 2004. High
682   pressure and high temperature phase transitions of FeO. Phys. Earth Planet. Int.
683   146, 273-282.

684 Ohtani, E., Yurimoto, H., Seto, S., 1997. Element partitioning between metallic liquid,
685   silicate liquid, and lower-mantle minerals: Implications for core formation of the
686   Earth. Phys. Earth Planet. Int. 100, 97-114.

687 Ricolleau, A., Fiquet, G., Addad, A., Menguy, N., Vanni, C., Perrillat, J.-P., Daniel, I.,
688   Cardon, H., Guignot, N., 2008. Analytical transmission electron microscopy study
689   of a natural MORB sample assemblage transformed at high pressure and high
690   temperature. Am. Mineral. 93, 144-153.

691   Righter, K., 2003. Metal-silicate partitioning of siderophile elements and core formation

692   in the early Earth. Annu. Rev. Earth Planet. Sci. 31, 135-174.

693   Righter, K., Drake, M.J., Yaxley, G., 1997. Prediction of siderophile element metal-

694   silicate partition coefficients to 20 GPa and 2800 °C: The effect of pressure,

695   temperature, fO_2 and silicate and metallic melt composition. Phys. Earth Planet.

696   Int. 100, 115-34.

697   Rubie, D.C., 1999. Characterizing the sample environment in multianvil high-pressure

698   experiments. Phase Transitions 68, 431-451.

699   Seagle, C.T., Heinz, D.L., Campbell, A.J., Prakapenka. V.B., Wanless, S.T., 2008.

700   Melting and thermal expansion in the Fe-FeO system at high pressure. Earth

701   Planet. Sci. Lett. 265, 655-665.

702   Shen, G., Mao, H.-k., Hemley, R.J., Duffy, T.S., Rivers, M.L., 1998. Melting and crystal

703   structure of iron at high pressures. Geophys. Res. Lett. 25, 373-376.

704   Shen, G., Rivers, M.L., Wang, Y., Sutton, S.R., 2005. Facilities for high-pressure research

705   with the diamond anvil cell at GSECARS. J. Synchrotron Rad. 12, 642-649.

706   Sinmyo, R., Hirose, K., Nishio-Hamane, D., Seto, Y., Fujino, K., Sata, N., Ohishi, Y.,

707   2008. Partitioning of iron between perovskite/postperovskite and ferropericlase in

708   the lower mantle. J. Geophys. Res. 113, B11204.

709   Stebbins, J.F., McMillan, P.F., Dingwell, D.B., 1995. Structure, Dynamics, and Properties

710   of Silicate Melts, Reviews in Mineralogy 32, Mineralogical Society of America,

711   Washington, DC.

712   Stixrude, L., Karki, B., 2005. Structure and freezing of $MgSiO_3$ liquid in Earth's lower

713   mantle. Science 310, 297-299.

714   Stølen, S., Grønvold, F., 1996. Calculation of the phase boundaries of wüstite at high

715   pressure. J. Geophys. Res. 101, 11531-11540.

716   Takafuji, N., Hirose, K., Mitomi, M., Bando, Y., 2005. Solubilities of O and Si in liquid

717   iron in equilibrium with $(Mg,Fe)SiO_3$ perovskite and the light elements in the

718   core. Geophys. Res. Lett. 32, L06313.

719   Thibault, Y., Walter, M. J., 1995. The influence of pressure and temperature on the metal-

720   silicate partition coefficients of nickel and cobalt in a model C1 chondrite and

721   implications for metal segregation in a deep magma ocean. Geochim.

722   Cosmochim. Acta 59, 991-1002.

723   Uchida, T., Wang, Y., Rivers, M.L., Sutton, S.R., Weidner, D.J., Vaughan, M.T., Chen, J.,

724   Li, B., Secco, R.A., Rutter, M.D., Liu, H., 2002. A large-volume press facility at

725   the Advanced Photon Source: Diffraction and imaging studies on materials

726   relevant to the cores of planetary bodies. J. Phys. Condens. Matter 14, 11517-

727   11523.

728   Wade, J., Wood, B.J., 2005. Core formation and the oxidation state of the Earth. Earth

729   Planet. Sci. Lett. 236, 78-95.

730   Walter, M.J., Newsom, H.E., Ertel, W., Holzheid, A., 2000. Siderophile elements in the

731   Earth and Moon: Metal/silicate partitioning and implications for core formation,

732   in: Canup, R.M., Righter, K. (Eds.) Origin of the Earth and Moon. Univ. of

733   Arizona, Tuscon, pp. 265-290.

734   Williams, Q., Jeanloz, R., 1988. Spectroscopic evidence for pressure-induced

735   coordination changes in silicate glasses and melts. Science 239, 902-905.

736   Zhang, F., Oganov, A.R., 2006. Valence state and spin transitions of iron in Earth's

737   mantle silicates. Earth Planet. Sci. Lett. 249, 436-444.

738

739

740

741 **Figure Captions**

742

743 Figure 1. Sample geometry and temperature distribution in the laser heated diamond

744 anvil cell experiments. The sample, a mixture of metal+oxide powders, was embedded in

745 a NaCl pressure medium that also acted as a thermal insulator and pressure standard,

746 using the equation of state for the B1 (Decker, 1971) or B2 (Fei et al., 2007) phases. The

747 temperatures were measured at the intersection of the x-ray beam with the two surfaces

748 of the opaque sample. Temperature distributions internal to the sample were calculated

749 by Campbell et al. (2007). The temperature profile across the NaCl insulator is

750 approximated as linear, with a mean temperature between that measured at the sample

751 surface (T_{meas}) and the diamond anvil, whose surface temperature is between T_{meas} and 295

752 K.

753

754 Figure 2. Equation of state data for Fe and FeO. Data below 15 GPa were obtained by

755 MAP; higher pressure data were obtained by DAC (this study and from Seagle et al.

756 (2008)). Squares: fcc-Fe; circles: hcp-Fe; triangles: FeO. Only the B1 phase of FeO was

757 observed in coexistence with Fe at high pressure and temperature. The data were

758 obtained only at P,T conditions sufficiently high to ensure stoichiometric $Fe_{1.000}O$ (Stølen

759 and Grønvold, 1996). Data are color coded to indicate temperature. Shown for

760 comparison are the Dewaele et al. (2006) equation of state for hcp-Fe and equations of

761 state from Table 1 at various temperatures. Each colored curve represents the midpoint of

762 the temperature range indicated.

763

764 Figure 3. Equation of state data for Ni and NiO. Data below 15 GPa were obtained by

765 MAP; higher pressure data were obtained by DAC. Circles: Ni; triangles: NiO. Data are

766 color coded to indicate temperature. A Mie-Grüneisen equation of state is fit to the data at

767   different temperatures as shown. Each colored curve represents the midpoint of the

768   temperature range indicated.

769

770   Figure 4. Volume differences between coexisting oxide and metal at high pressures and

771   temperatures, from the data in Figures 2 and 3. Diamonds: FeO-fcc Fe; circles: FeO-hcp

772   Fe; squares: NiO-Ni.

773

774   Figure 5. (a) Fe-FeO and (b) Ni-NiO oxygen fugacity buffers, and (c) the difference

775   between them, at various pressures. The 1 bar buffer curves were calculated from Chase

776   (1998) and Knacke et al. (1991), and high pressure curves were calculated from Equation

777   (6) using fits to the data like those in Figures 2 and 3. With increasing pressure and

778   temperature, the difference between the Ni-NiO and Fe-FeO buffers decrease, indicating

779   decreasing siderophility of Ni. Uncertainties are indicated in (c) by vertical bars.

780

781   Figure 6. Fe-FeO and Ni-NiO oxygen fugacity buffers along a representative geotherm

782   through the Earth's mantle (Brown and Shankland, 1981; Dziewonski and Anderson,

783   1981). At 2000 km depth, the pressure and temperature are 86.9 GPa and 2256 K. The

784   difference between the two buffers decreases from 5.0 log units at 1 bar, 1400 K to 2.1

785   log units at 2000 km depth.

786

787   Figure 7. Exchange coefficient (K_D) for Ni and Fe between metallic melt and peridotitic

788   silicate at high pressure. Shaded circles: Li and Agee (1996). Open squares: Ito et al.

789   (1998). Solid curve: calculated pressure dependence based on equation (10) and

790   experimental equation of state results of this study, assuming that the activity coefficient

791   term in eqn. (10) is constant with pressure. The curve predicts the pressure dependence at

792   low pressures, but above 10 GPa the curve deviates from the data, suggesting nonideal

793   mixing related to changes in the silicate melt structure. Dashed curve: shows the effect of

794   a mixing volume of -1.5 cm^3/mol applied above 10 GPa.

795

Table 1. Equation of state (Birch-Murnaghan) parameters.

	Fe-fcc	FeO-B1	Ni	NiO
V_0, cm^3/mol	7.076 [a]	12.256 [b]	6.587 [a]	10.973 [a]
K, GPa	133 ± 3	146.9 ± 1.3	179 ± 3	190 ± 3
K'	5 [c]	4 [d]	4.3 ± 0.2	5.4 ± 0.2
Θ_D, K	470 [e]	380 [e]	415 [f]	480 [f]
γ_0	1.95 ± 0.04	1.42 ± 0.04	2.50 ± 0.06	1.80 ± 0.04
q	1.6 ± 0.6	1.3 ± 0.3	1	1

Entries in italics held fixed in the fit:
[a]JCPDS card files.
[b]McCammon, 1984.
[c]Funamori et al., 1996.
[d]Fei, 1996.
[e]Chase,1988.
[f]Knacke et al., 1991.
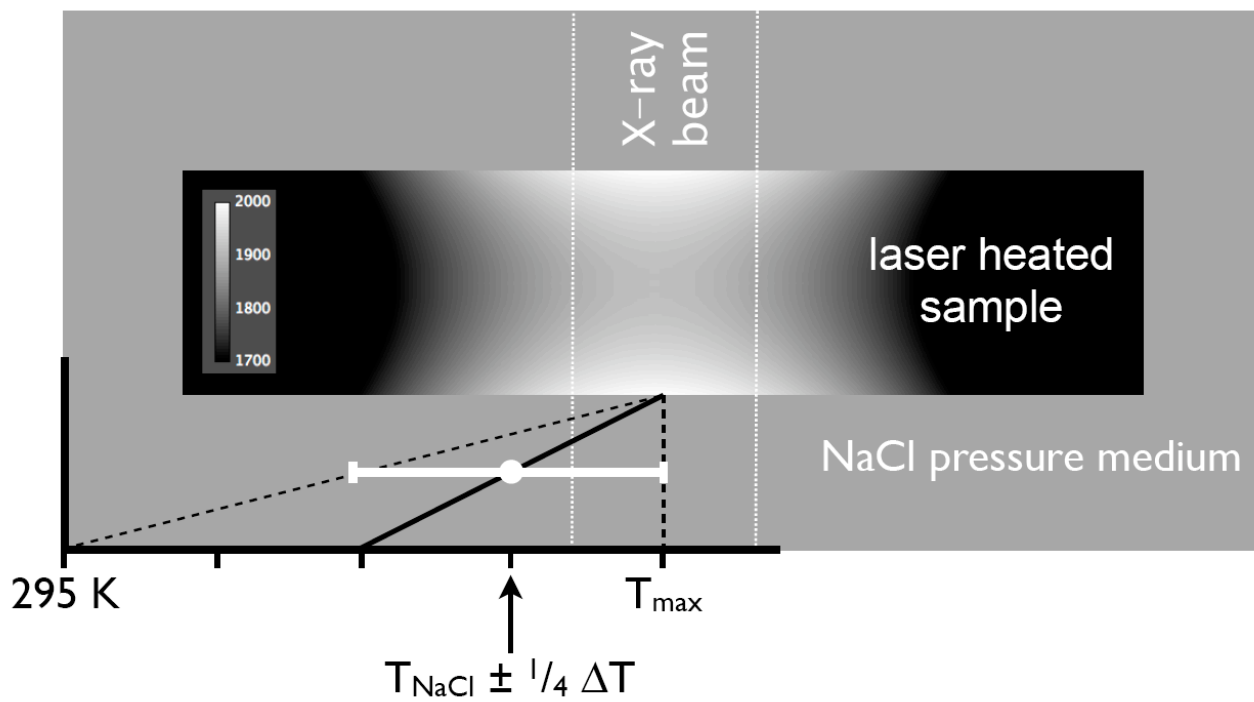
Figure 1
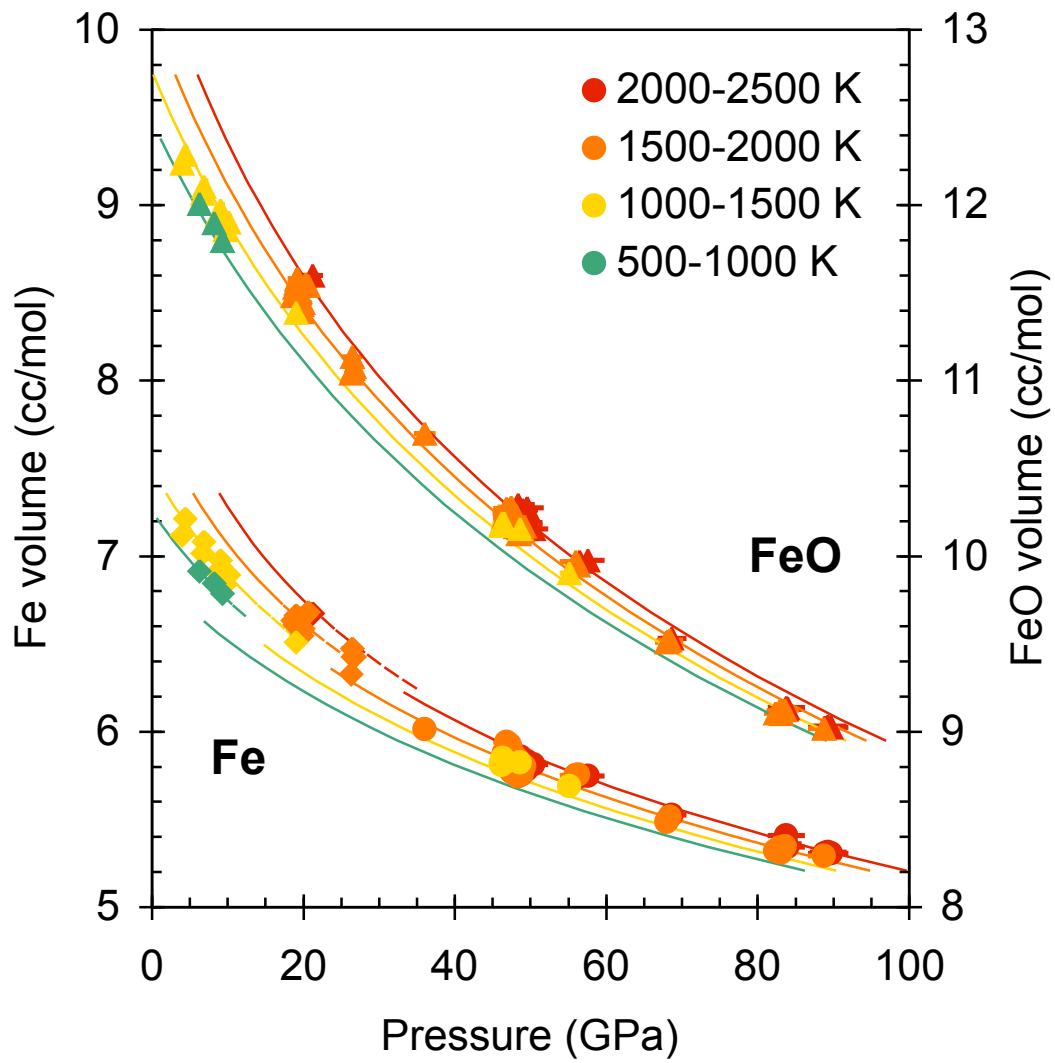
Figure 2
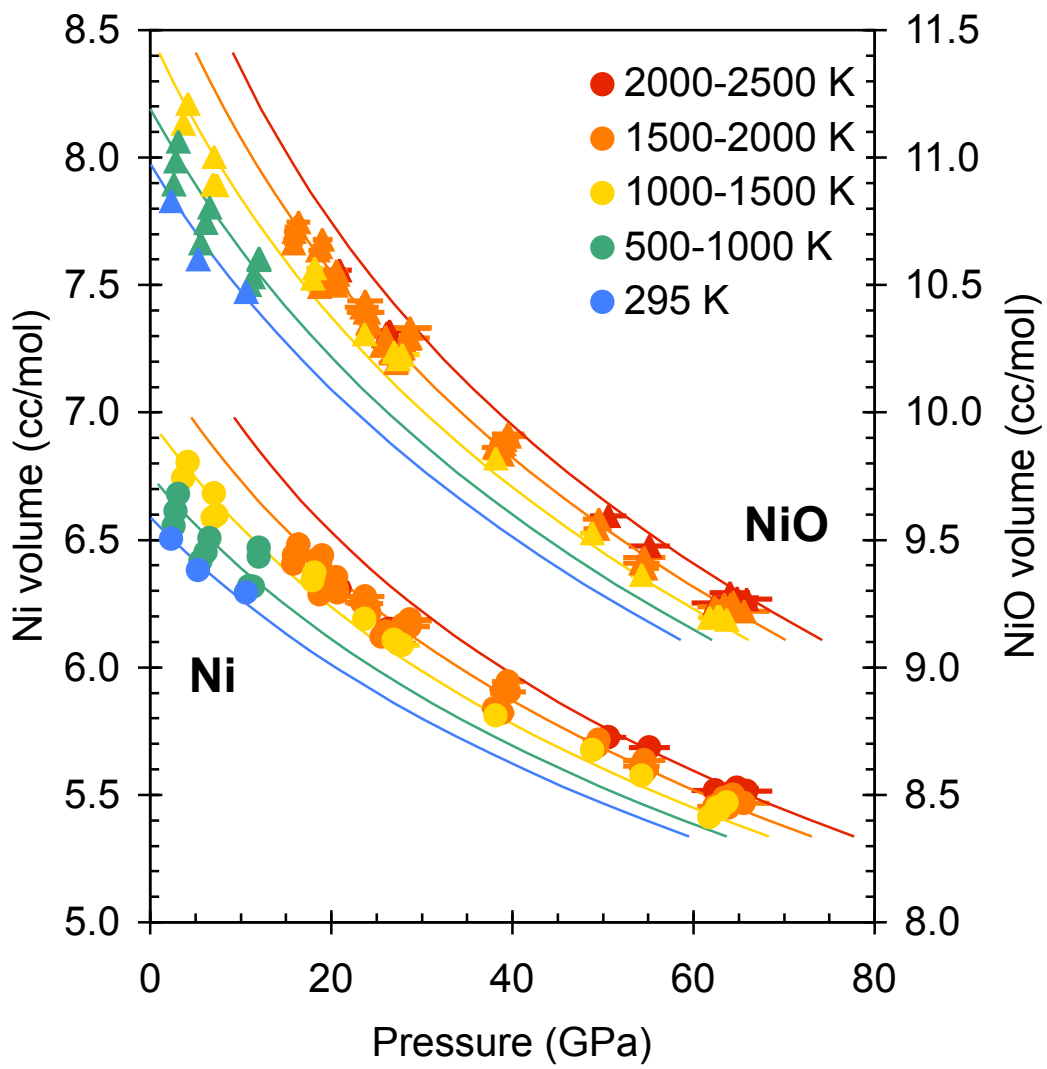
Figure 3
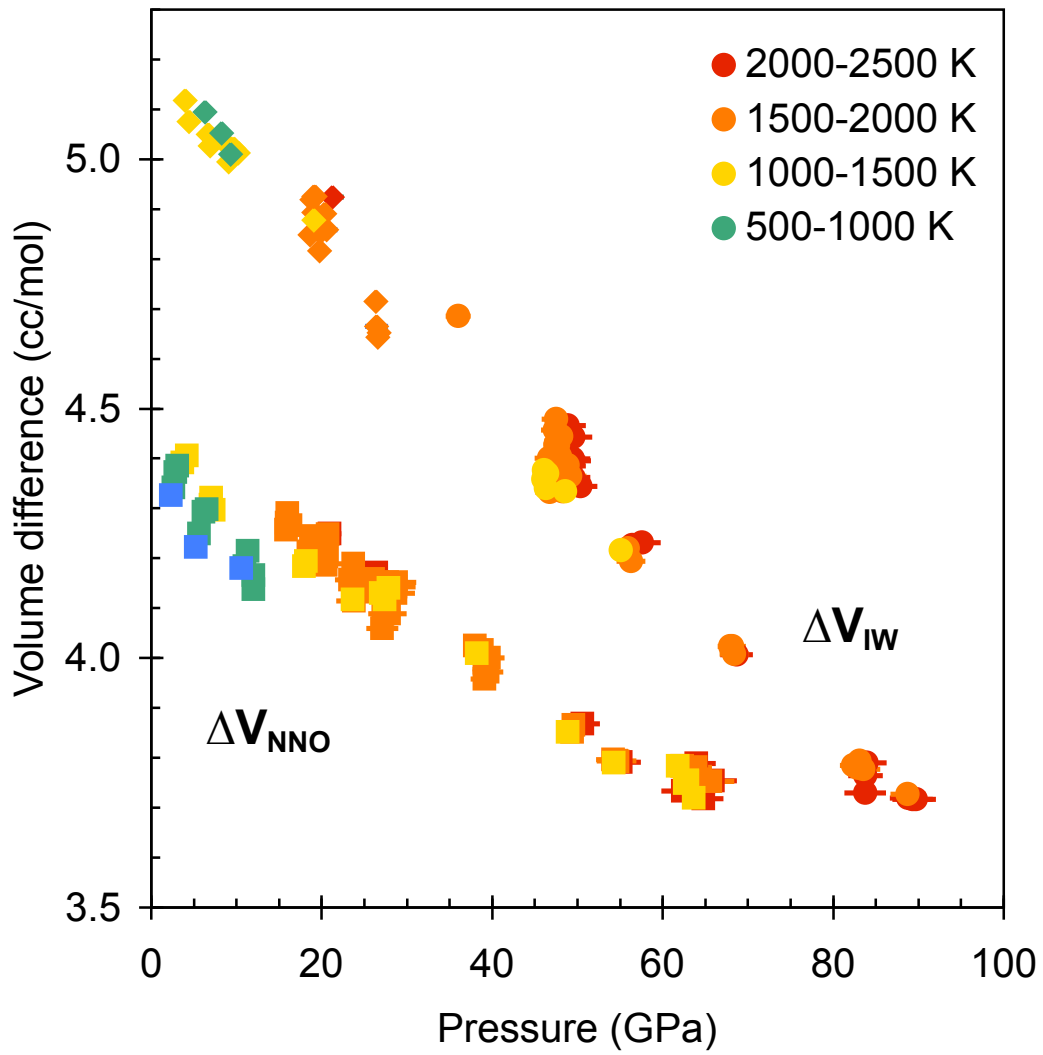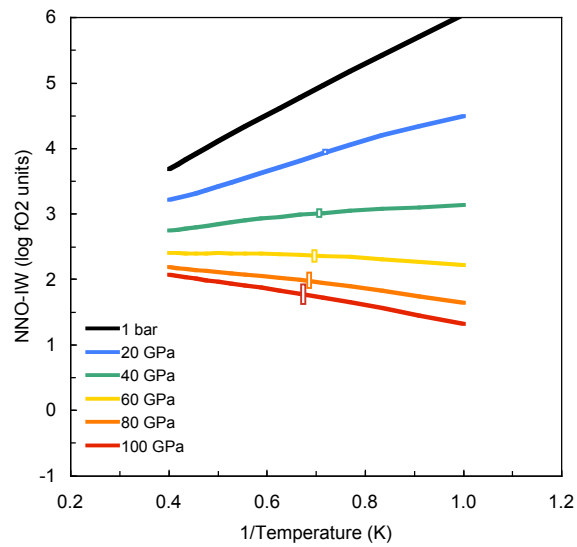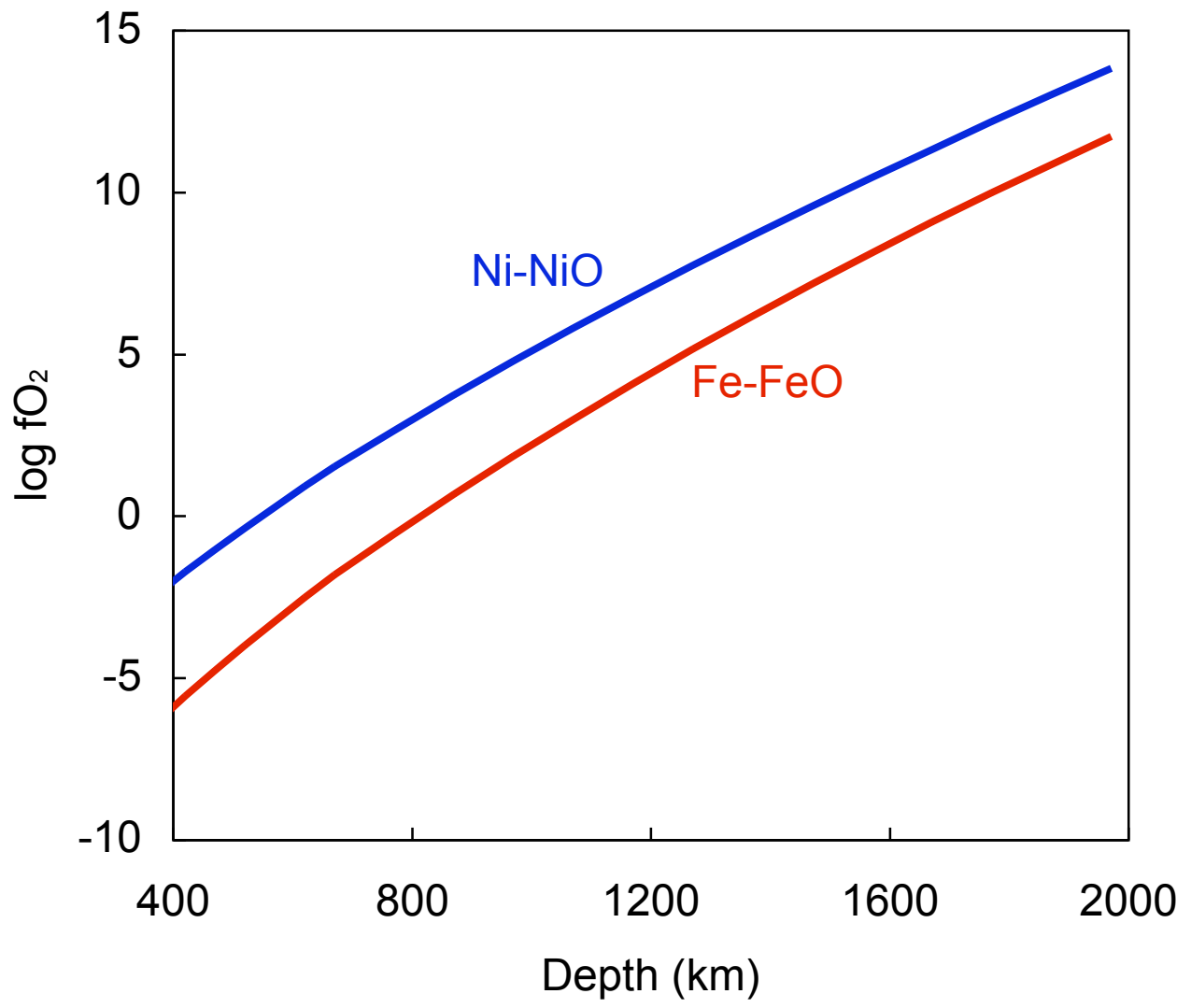
Figure 4
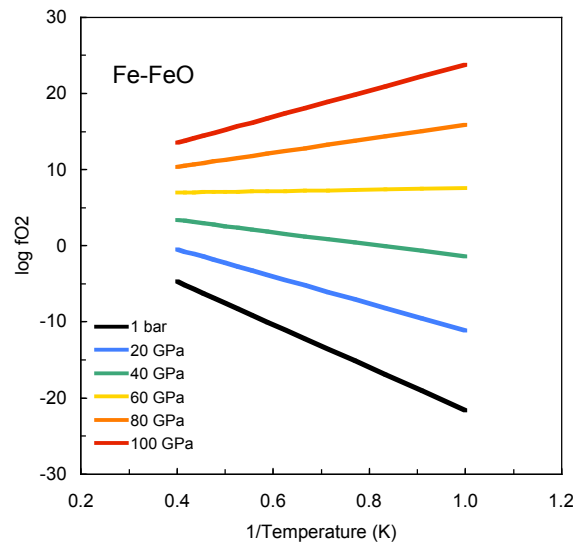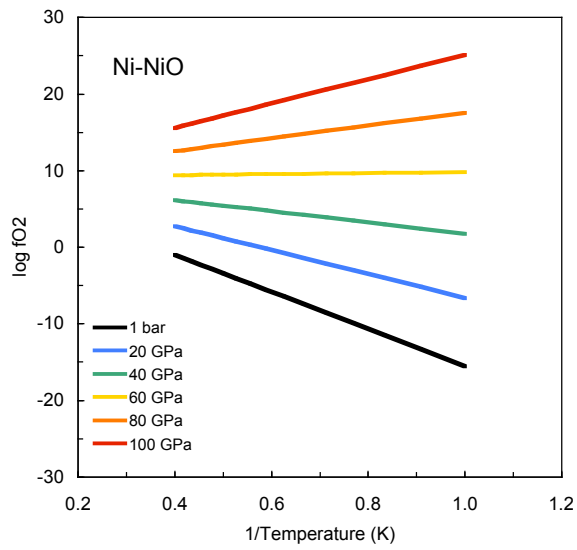
Figure 5

Figure 6
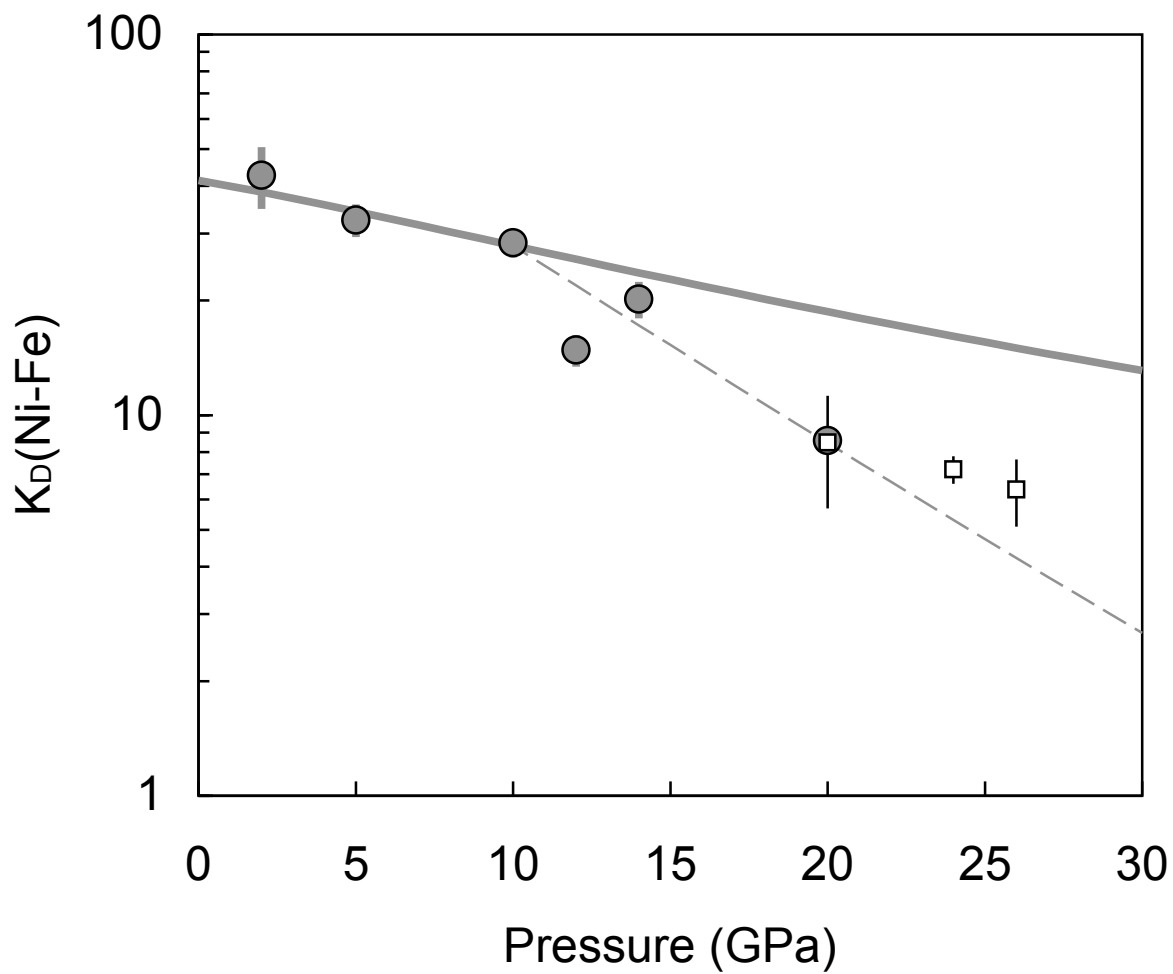
Figure 7

Supplementary Material

Supplementary Figure S1. Representative X-ray diffraction data obtained while laser heating a Ni+NiO sample in a diamond anvil cell. The graph shows the diffraction pattern obtained by azimuthal integration of the 2-D diffraction image. The white region in the center is caused by a beam stop blocking the primary X-ray beam. Inset: X-ray diffraction image. The spottiness of the diffraction rings is a consequence of recrystallization upon heating.

Supplementary Table S2. Pressure-volume-temperature data from X-ray diffraction experiments on Fe+FeO.

Supplementary Table S3. Pressure-volume-temperature data from X-ray diffraction experiments on Ni+NiO.

Supplementary Table S4: Fe-FeO oxygen fugacity buffer from 1000 to 2600 K and 0 to 100 GPa.

Supplementary Table S5: Ni-NiO oxygen fugacity buffer from 1000 to 2600 K and 0 to 100 GPa.
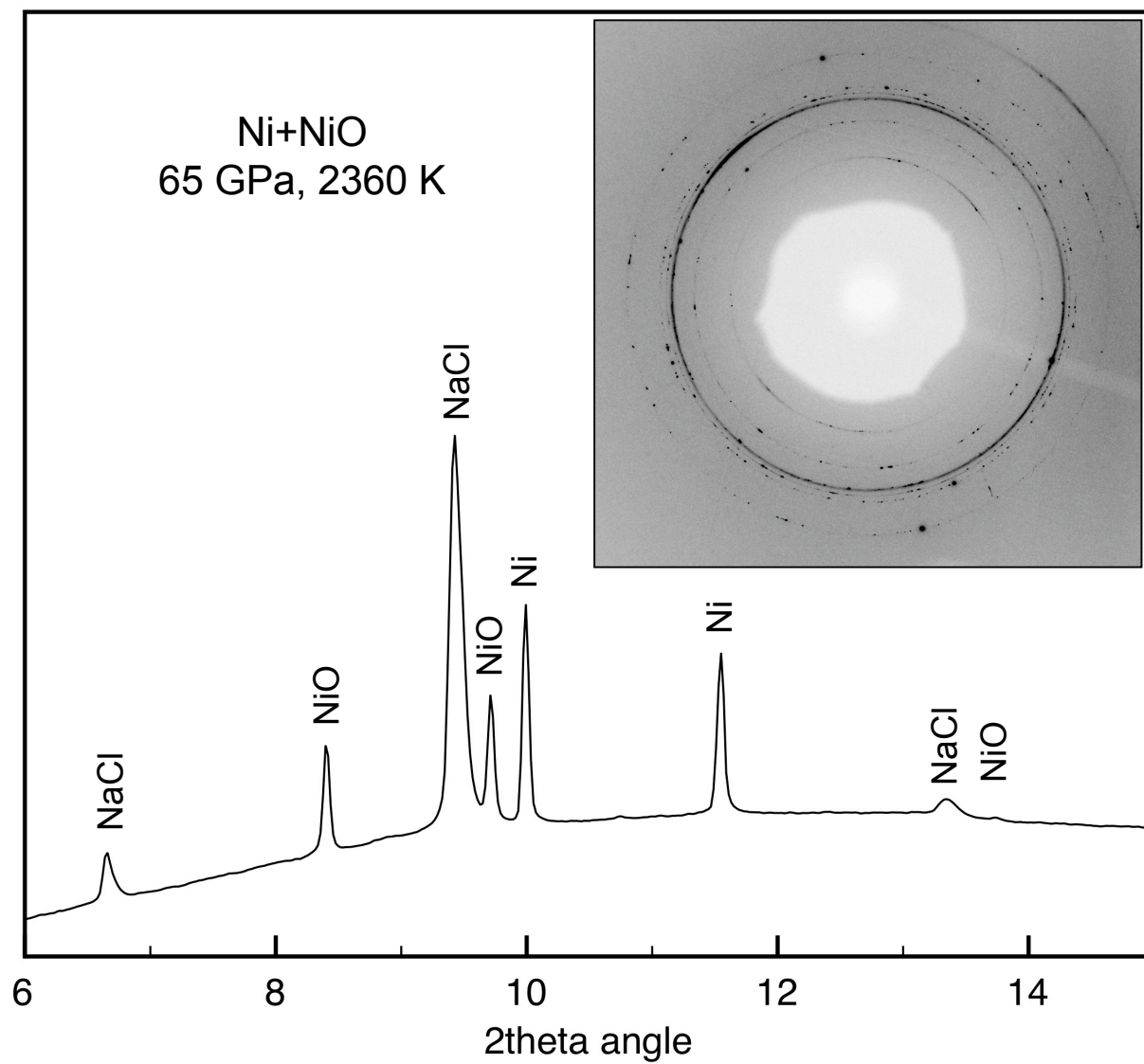
Figure S1